ARTICLE IN PRESS

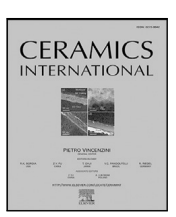
Ceramics International xxx (xxxx) xxx

ELSEVIER

Contents lists available at ScienceDirect

Ceramics International

journal homepage: www.elsevier.com/locate/ceramint



Heat radiation mitigation in rare-earth pyrosilicate composites: A first principles investigation of refractive index mismatch

Sara Kadkhodaei*, Seyyedfaridoddin Fattahpour, Ali Davariashtiyani

Department of Civil, Materials, and Environmental Engineering, University of Illinois Chicago, Chicago, IL, USA

ARTICLE INFO

Keywords: Thermal radiation Refractive index mismatch Ceramic composites Rare earth pyrosilicates Pyrochlore rare-earth hafnate and zirconate

ABSTRACT

Thermal radiation emission poses a challenge for using most existing ceramics for thermal environmental barrier coatings of gas-turbine engines operating at temperatures approaching 1500 °C and beyond. This study presents a strategy for photon transport mitigation in fully dense ceramic composites by increasing the refractive index mismatch between the matrix and particle oxides. We investigate this strategy by analyzing radiative properties in 118 different rare-earth pyrosilicate–pyrochlore ceramic composites. We use density functional theory to predict the optical properties of homogeneous oxides and Lorentz–Mie theory to model scattering at the interfaces of the composite. Our findings demonstrate that increasing the refractive mismatch between the matrix and oxide phases can significantly reduce radiative heat flux. Furthermore, we show that additional thermal radiation suppression can be achieved by increasing the particle size. Our theoretical investigation has the potential to aid in the discovery of new coating ceramic composites and guide their microstructural design.

1. Introduction

Gas-turbine (GT) engines with ceramic-matrix composite (CMC) hot section components are expected to operate at gas-inlet temperatures approaching 1700 °C [1-4]. At temperatures above 1700 °C, ceramics start to emit thermal radiation in the visible and near-infrared regions of the electromagnetic spectrum. However, the current coating materials are partially transparent to visible and near infrared radiation at these temperatures. This makes the radiative heat flux (which scales with T^4) the major bottleneck for their use, even though they have low thermal conductivities [1,5–14]. The push for increased operating temperatures has limited the choice of current materials of use for thermal barrier coatings to a few high-temperature ceramics [3,15]. There is a clear need to identify and optimize coating materials that can reduce radiative heat fluxes. In general, radiative heat transfer was not considered explicitly in many of the heat transfer studies in thermal barrier coatings (TBCs). More recent studies have analyzed heat transfer in ceramic coatings considering the radiative flux [16-22], knowing that the operation temperature of next-generation coatings are expected to approach 1500 °C and above.

For porous coating materials, like porous zirconia and alumina produced by plasma-spraying technology, radiation scattering tends to dominate over absorption [17]. Generally, the effect of pores in phonon and photon scattering is significant and has been well studied [2,18,23–31]. Thereby, tailoring porosity, both in magnitude and distribution, is

the main strategy for radiation and conduction mitigation for porous coatings. Flamant and Clark have recently outlined some guidelines for radiative heat mitigation in ceramic coatings through a combination of atomic level doping and scattering [32]. Another group of coating materials that has recently attracted interest are fully dense ceramics for multifunctional thermal environmental barrier coatings (TEBCs) [20,21,33,34]. In the absence of porosities to scatter photons in fully dense ceramics, alternative strategies for photon scattering have been investigated [20,21]. For example, J. Yang et al. found that addition of LaPO₄ as a second phase in the La₂Zr₂O₇ matrix led to a percolating interconnected network inside the material, resulting in a remarkable reduction of infrared radiation [20]. In a more recent study, H. Aziz et al. observed high-temperature photon suppression in a ceramic composite consisting of 8 wt% yttria-stabilized zirconia (8YSZ, matrix) and corundum (second component) due to a smaller refractive index of the second phase for a controlled particle size [35].

Experimental measurements of radiative properties and thermal radiation can be challenging and time consuming due to difficulties in accurate temperature control, isolating the radiation from background radiation, and measurement accuracy. Due to these difficulties, studies that explicitly report the radiative heat transfer and measure radiative properties are few. These difficulties pose a barrier for a high-throughput investigation of new ceramics with enhanced heat radiation

E-mail address: sarakad@uic.edu (S. Kadkhodaei).

https://doi.org/10.1016/j.ceramint.2024.01.417

Received 28 October 2023; Received in revised form 17 January 2024; Accepted 30 January 2024 Available online 1 February 2024

0272-8842/© 2024 The Author(s). Published by Elsevier Ltd. This is an open access article under the CC BY-NC-ND license (http://creativecommons.org/licenses/by-nc-nd/4.0/).

^{*} Corresponding author.

mitigation. In this study, we perform a high-throughput ab initio investigation of the explicit radiative properties of rare-earth pyrosilicatepyrochlore composite ceramics. Rare-earth pyrosilicate ceramics have shown promise as a new class of coating materials for thermal environmental barrier coatings on CMCs [33,34,36]. We investigate photon transport (or radiation) in fully dense ceramics, examining it at both the fundamental level of electronic excitations (using density functional theory) and the microstructural level (using Lorentz-Mie theory). Our results show that thermal radiation is mitigated by increasing the optical mismatch between phases in multi-phase ceramic composites. Our results also indicate that additional thermal radiation suppression can be achieved by increasing the particle size, noting that our theoretical analysis is limited by an upper bound for the particle size and density – a 1 um particle size per cubic micron of matrix – where the independent scatter assumption is valid. Our results provide guidance for the design of radiative heat transfer in TEBCs and lay the foundation for further studies on radiative heat transfer in these materials.

This study consists of three main parts: (1) First-principles calculations of optical properties of homogeneous media of rare earth pyrochlores (A2B2O7) and pyrosilicates (A2Si2O7). Based on ab initio electronic structure calculations, we predict the spectral distribution of the optical properties (absorption, reflectivity, and refraction index) for several rare-earth (RE) pyrochlores and pyrosilicates, and we identify ceramics with large attenuation coefficients. The effect of different RE elements on the attenuation coefficient is shown. These results provide new insights into combination of rare-earth elements that can widen the absorption in the visible and infrared spectrum. (2) We study several ZrO2 and HfO2 based pyrochlore oxides for the second phase in ceramic composites with RE pyrosilicate matrices. We show that by contrasting the refractive indices of the matrix ceramic and the second-phase oxide, enhanced radiation scattering is achieved, rendering the ceramic composite opaque. Accordingly, optimized two-phase microstructures for large internal reflections (or scattering) are identified. The relative refraction index between various pairs of oxide phases is predicted from ab initio while the radiative reflections for the composite is analytically modeled using the Lorentz-Mie theory. We predict the effective radiation conductivity using the diffusion approximation of radiation. These methods are detailed in Section 2. (3) We investigate radiation scattering in different composites of different particle sizes. We modify the size of embedded particles in different composites and use Mie theory predictions to study the change in scattering and attenuation characteristics within the composite. We predict the effective radiation conductivity for different sizes of particles in the composites.

Our *ab initio* calculations show that significant thermal radiation resistance is achieved in two-phase ceramic composites by both increasing radiation scattering in individual phases and by enhancing internal radiation reflection at the two-phase interfaces. The fundamental insights and predictions from our theoretical studies will be instrumental in discovery of new coating ceramic composites and guiding their experimental design. Considering the huge design space for novel ceramics, this study presents a systematic approach to identify entirely new optically thick ceramics with enhanced thermal radiation trapping.

2. Methods

2.1. First-principles calculations of optical properties

The intrinsic optical properties of homogeneous oxides are derived from the fundamental dielectric function. The dielectric function is the linear electronic response function, which describes the electron displacement generated by an incident electric field. The spectral dielectric function is obtained through electronic structure calculations within density functional theory (DFT) [37], as detailed below. The dielectric function, denoted as $\bar{e}(v) = \epsilon_r(v) + i\epsilon_i(v)$, is a unitless complex

function with real and imaginary parts, represented by ϵ_r and ϵ_i , respectively. It depends on the radiation frequency (or wavelength), denoted by ν (or λ). The dielectric function is directly related to the spectral optical properties of individual (homogeneous) oxides, including the complex refractive index denoted as $\bar{n}=n-i\kappa$, through the Maxwell equations:

$$n = \frac{\sqrt{\epsilon_r + |\bar{\epsilon}|}}{\sqrt{2}} \quad , \quad \kappa = \frac{\sqrt{-\epsilon_r + |\bar{\epsilon}|}}{\sqrt{2}}$$
 (1)

Here, n and κ are the real and imaginary parts of the complex refractive index, respectively, and $|\bar{\epsilon}|$ depicts the magnitude of the complex dielectric function. The absorption of the electromagnetic wave (or radiation) is obtained from the imaginary part of the complex refractive index according to $\alpha = \frac{4\pi\kappa}{\lambda}$. The absorption coefficient has a unit of inverse length. The reflectivity R describes the interaction of radiation wave with the oxide boundary, which is related to the components of the complex refractive index by Snell's law. The reflectivity of the oxide in vacuum is calculated as $R = \frac{(n-1)^2 + \kappa^2}{(n+1)^2 + \kappa^2}$ and is unitless. The DFT calculation of the dielectric function, $\bar{\epsilon}$, is performed

The DFT calculation of the dielectric function, \bar{e} , is performed using the Vienna Ab-initio Simulation Package (VASP) [38–40]. We employ the projector-augmented-wave (PAW) method [41,42] and the generalized gradient approximation (GGA) with the Perdew–Burke–Ernzerhof (PBE) exchange–correlation [43]. A self-consistent ground-state electronic structure calculation is performed, followed by the dielectric function calculation. To calculate the spectral dielectric function, we employ the independent-particle approximation as implemented in VASP [44]. The energy threshold is set to 5×10^{-5} eV per atom for the electronic self-consistent loop. The energy cutoff is set to 520 eV. The k-point density is set to 100 and 400 per inverse \forall 3 of reciprocal cell for the ground-state and dielectric calculations, respectively. All calculations include spin polarization of electrons but spin–orbit coupling is not considered.

Rare earth pyrochlores have the cubic $Fd\bar{3}m$ space group (number 227) with the reduced formula of $(RE)_2(Hf,Zr)_2O_7$. The generated pyrochlores have a 22-atom supercell with a full formula of $A_4B_4O_{14}$. The A site contains a rare-earth element where the B site is occupied by either Hf or Zr. Rare earth pyrosilicates have the monoclinic crystal structure with the reduced formula of $(RE)_2(Si)_2O_7$. The pyrosilicates in this study have space groups $P2_1/c$, C2/m, or $P2_1/m$ with corresponding supercell sizes of 22 (or 44), 11, and 22 atoms, respectively. Supplemental Table S1 provides comprehensive information on the supercell configurations of rare-earth pyrochlores and pyrosilicates examined in this study.

The dielectric function arises from potential excitations within a solid material when subjected to an external electric field. These potential excitations manifest differently based on the energy range of the incident radiation. Notably, visible light and near-infrared radiation are situated within the lower-energy segment of the spectral range ($h\nu$ < 3 eV). In the lower range, excitations such as magnetic interactions, lattice vibrations, free carrier absorption, and polarization of valence electrons significantly shape the dielectric function [45]. In contrast, in the higher energy spectrum (where hv > 5 eV), the primary excitations shift to include excitons, absorption across the band gap, inter-band transitions, transitions to higher bands, and transitions from core levels. Our focus here is on investigating the optical properties of ceramic oxides within the visible and near-infrared range. Consequently, inter-band transitions and excitons across the band gap have reduced significance. Therefore, the level of DFT theory employed in this study adequately accounts for the predominant excitations within the visible light and near-infrared energy range.

To demonstrate the reliability of the DFT level used in this study, Supplemental Figure S1 compares the calculated spectral dielectric function for ${\rm Er_2Si_2O_7}$, ${\rm Ho_2Zr_2O_7}$, and ${\rm Dy_2Hf_2O_7}$ with higher-level DFT calculations that include spin–orbit coupling or the random phase approximation (RPA) [46,47]. For this comparison, a 4 × 4 × 4 k-point

mesh is used to reduce the computational cost. As shown in Supplemental Figure S1, the IPA demonstrates reasonable accuracy in predicting the dielectric function and resulting optical properties, particularly within the visible light and near-infrared radiation range ($h\nu < 3$ eV) — a range pertinent to thermal coating applications targeted in this study. We should note that the accuracy of DFT calculations can be furthered increased, albeit with a higher computational cost, by utilizing hybrid functionals [48] instead of the generalized gradient approximations (GGA) functionals [49]. Considering the high-throughput nature of this study, we choose the less computation-intensive, yet reasonably accurate GGA functionals with IPA for the DFT calculation of the dielectric function.

2.2. Lorentz-mie model for radiation scattering in ceramic composites

To study radiation in two-phase oxide composites, the effect of microstructure heterogeneities, including surfaces and interphase interfaces, must be included. Specifically, internal radiative reflections at two-phase interfaces (i.e., scattering) can become significant and render the composite more opaque compared to homogeneous oxides. We investigate the effect of an increased refractive index mismatch between the matrix and particle oxides on radiation scattering in the ceramic composite. We employ the Lorenz-Mie theory (LMT) [50,51], as implemented in the miepython package [52], to predict radiation scattering at the interphase interfaces of the matrix and particle oxides. LMT provides an analytical solution of the electromagnetic-wave interaction (or scattering) with spherical particles, i.e., it is assumed that the second phase particles are spherical with specular surfaces. Additionally, LMT assumes that the scattering medium (or the matrix oxide in this case) is isotropic and its refractive index remains constant throughout the scattering process and across the medium. Here, we study fully dense ceramic composites with no porosity. Thereby, the scattering medium is the matrix oxide phase and the second-phase spherical oxide particles are embedded within the matrix oxide. The LMT solutions give us the so-called spectral absorption and scattering cross sections, C_a and C_s , which refer to an effective particle area (with units of area) that removes the electromagnetic wave energy from the path of the incident radiation. The unit-less efficiency factors, Q_a or Q_s , are obtained by dividing the absorption and scattering cross sections with the actual geometric cross section of the particle (see Eq. 15.32 in

To make the predictions of scattering behavior of the composite oxide valid within the Lorentz–Mie theory, the particles should be single scatterers, where the scattered light is assumed to undergo only one scattering event. Therefore, the arrangement of particle oxides within the matrix oxide is assumed to be monodispersed with a large enough distance between particles. For spherical particles, scattering is found to be independent if the following criterion is met, $c+0.1D > \frac{1}{2}\lambda_m$ (see Eq. 15.57 of Ref. [51]). Here, c is the clearance distance between particles, D is the particle diameter, and λ_m is the wavelength in the medium (= $\lambda/n_{\rm medium}$).

For a cloud of monodispersed oxide particles embedded into the matrix oxide, the spectral absorption and scattering coefficients $\sigma_{\lambda,a}$ and $\sigma_{\lambda,s}$ are calculated from the efficiency factors by

$$\sigma_{\lambda,a} = NQ_{\lambda,a}\pi \frac{D^2}{4} \quad , \quad \sigma_{\lambda,s} = NQ_{\lambda,s}\pi \frac{D^2}{4} \tag{2}$$

where D is the particle diameter and N denotes the number of particles per unit volume, expressed in units of reciprocal volume. The attenuation of radiation due to absorption and scattering can be effectively described by the extinction or attenuation coefficient, $\beta_{\lambda} = \sigma_{\lambda,a} + \sigma_{\lambda,s}$, which sums the absorption and scattering coefficients. These coefficients have units of reciprocal length. β_{λ} can be interpreted as the inverse of the mean penetration distance of radiation or the so-called mean free path of radiation $I_{\lambda} = 1/\beta_{\lambda}$. To satisfy the independent (or single) scatterer assumption, we adopt a sufficiently small N value for

the mean distance between the particles to be larger than the incident wave length in the visible and near-infrared range. Accordingly, we study a ceramic composite that contains one particle of diameter D per cubic micron of the matrix oxide (i.e., N=1 µm⁻³).

In addition to the absorption and scattering coefficients, we obtain the scattering phase function, Φ , which gives the probability that an incident light on a particle at a given direction being scattered into another direction. The scattering angle is a solid angle of unit steradian and is defined as the angle between the incident and scattered directions. For the study of composites, we assume that azimuthal symmetry exists; therefore the phase function is expressed only in terms of the polar angle $\Phi(\theta)$.

2.3. Diffusion method for thermal radiation

Radiation of heat is viewed as the propagation of quanta of electromagnetic waves or photons in the matter [53,54]. Photons interact with absorbents and scatterers, e.g., particles, molecules, impurities, voids, or any inhomogeneities, in the form of absorption, re-emission, and multiple internal reflections (a.k.a. scattering) from internal boundaries, interfaces, and surfaces. The net effect of these absorptions and scatterings is radiation resistance or radiation intensity reduction within the ceramic [54]. The concept of mean free path for both phonons and photons has been employed to conveniently quantify thermal conduction and radiation in ceramics [53,54]. By analogy with the kinetic theory of gases, phonon thermal conductivity in ceramics is given by the general equation of $k_p = \frac{1}{3}C_\lambda v_\lambda l_\lambda^p$ where C_λ is the heat capacity, v_λ is the phonon velocity and l_λ^p is the phonon mean free path. A similar analogy between the kinetic theory of heat conduction and photon radiation can also be derived, which is outlined below.

In coating applications, ceramics are usually assumed to be optically thick or opaque, where radiation only travels a short distance before being scattered or absorbed. In other words, it is assumed that the mean free path of photons is relatively small. For such optically thick media, radiative transfer is similar to heat conduction with a temperature-dependent thermal conductivity and can be readily combined with heat conduction. This is called the diffusion approximation for radiation, under which the complex integral form of radiative transfer equation (RTE) is transformed into a diffusion-like relation (see Eq. 12.30 of Ref. [51]), where the total radiative flux q_r is given by

$$q_r(x) = -\left[\frac{16}{3\beta_R}\sigma_{SB}T^3\right]\frac{dT}{dx} = -k_r\frac{dT}{dx} \tag{3}$$

where σ_{SB} is the Stefan–Boltzmann constant, β_R is the mean radiation attenuation coefficient, and the term in the bracket is the effective radiation conductivity, k_r , in the diffusion approximation for radiation. The main assumptions in the diffusion approximation for radiation are isotropic scattering, or isotropic radiation intensity in general, and simplifying the 3D nature of heat radiation to unidirectional transport. Additionally, heat radiation in ceramic coatings is described by averaging the wavelength or spectral dependence of absorption, scattering, and attenuation coefficients, i.e., using average wavelength-independent σ_a , and σ_s , and β [51]. We use the local Rosseland mean attenuation coefficient, β_R , as the average radiation attenuation coefficient, defined as (see Eq. 12.34 of Ref. [51])

$$\frac{1}{\beta_R} = \int_{\lambda=0}^{\infty} \left(\frac{1}{\beta_{\lambda}}\right) \left(\frac{\partial E_{\lambda b}}{\partial E_b}\right) d\lambda \tag{4}$$

where β_{λ} is the spectral attenuation coefficient and $E_{\lambda b}$ and E_b are the spectral and total hemispherical emissive power of the blackbody radiation in vacuum, respectively.

More sophisticated approximations have been employed to described radiation heat fluxes in coating materials [55], such as the two-flux [56,57] and four-flux methods [16,58,59]. These methods are approximations to a more general class of multi-flux methods for solving the RTE, with the main assumption of isotropic radiation intensity [51], among other methodologies [22,31]. In most studies in

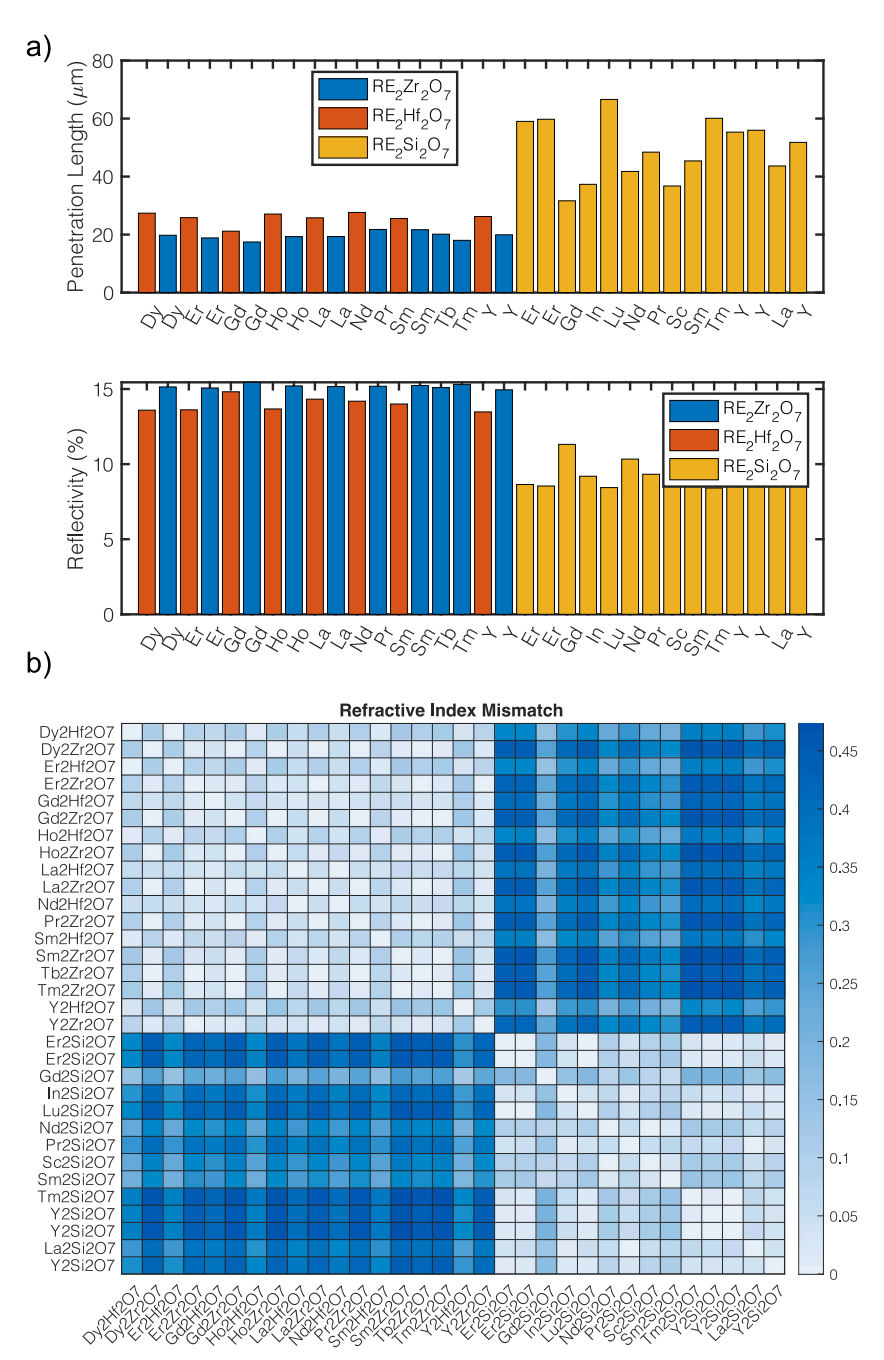


Fig. 1. (a) The average penetration length and reflectivity of pyrochlores $RE_2Zr_2O_7$ and $RE_2Hf_2O_7$ and pyrosilicates ($RE_2Si_2O_7$) in the visible light and infrared range. (b) The magnitude of the refractive index mismatch between pairs of pyrochlores and pyrosilicates.

the literature, the common approach for quantifying radiation and conduction heat in coatings is mostly empirical. For example, absorption and scattering coefficients for ceramics coatings are determined from the experimentally measured hemispherical-directional reflectance and transmittance values [59].

3. Results and discussion

3.1. Optical properties of homogeneous oxides

The spectral dielectric function is calculated for the target oxides, the pyrochlores and pyrosilocates listed in Supplemental Table S1, using DFT as detailed in Section 2. The optical properties of the homogeneous medium of these oxides are then calculated from the spectral dielectric function, as explained in Section 2. These optical properties

include the complex refractive index \bar{n} , the absorption coefficient α , and reflectivity R. Supplemental Figure S2 shows the calculated dielectric function and complex refractive index for the pyrochlores and pyrosilocates of this study. The calculated refractive indices for $\mathrm{Gd}_2\mathrm{Zr}_2\mathrm{O}_7$, $\mathrm{La}_2\mathrm{Zr}_2\mathrm{O}_7$, and $\mathrm{Y}_2\mathrm{Hf}_2\mathrm{O}_7$ exhibit good agreement with experimental data from the literature [21,60,61], as illustrated in Supplemental Figure S3. The DFT results slightly overestimate the real part of the refractive index in all three pyrochlore oxides. Nevertheless, DFT successfully replicates the relative spectral dependence across the three oxides. Supplemental Figure S4 shows the absorption coefficient α and reflectivity R for individual homogeneous oxide phases. To better compare the optical properties of different pyrochlores and pyrosilocates, Fig. 1(a) illustrates the penetration length, which is the inverse of the absorption coefficient α , and the reflectivity of radiation in homogeneous oxides, averaged over the visible light and infrared spectrum, with

Two-phase Composite TEBC

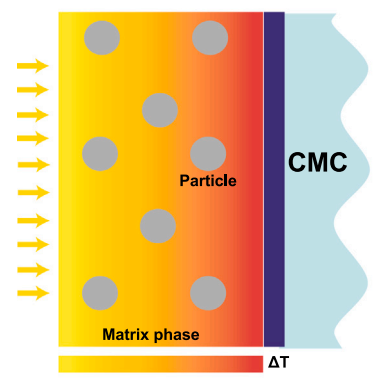


Fig. 2. A schematic illustration of a fully dense two-phase oxide composite for thermal environmental barrier coating (TEBC) application on ceramic-matrix composite (CMC) hot sections of gas-turbine engines. The particles are mono-dispersed in the matrix oxide phase. In this study, the RE pyrosilicates and pyrochlores constitute the matrix phase and particles, respectively.

wavelengths ranging from 0.4 to 3.3 µm. The average is calculated according to $\langle f \rangle = \frac{\int_{0.4}^{3.3} f d\lambda}{3.3-0.4}$ for both absorption coefficient and reflectivity. Rare-earth pyrochlores exhibit smaller penetration lengths (or higher absorption of radiation) and greater reflectivity when compared to pyrosilicates. Among the rare-earth pyrochlores, rare-earth zirconates are more opaque compared to rare-earth hafnates because they exhibit smaller penetration length and larger reflectivity.

The distinctive absorption and reflectivity behaviors observed in pyrosilicates and pyrochlores render them excellent candidates for the matrix phase and particle constituents within a composite ceramic (as detailed in Section 3.2). Fig. 1(b) shows the difference in the magnitude of the complex refractive index, $|\bar{n}|$, among various pairs of rare-earth pyrochlores and rare-earth pyrosilicates. The disparity in refractive indices between pyrochlores and pyrosilicates is notably greater than that observed among oxides within these respective groups (see Supplemental Figure S5). The most substantial refractive index mismatches are found in the following pairs, listed in order of magnitude: $Gd_2Zr_2O_7$ - $Lu_2Si_2O_7$, $Gd_2Zr_2O_7$ - Gd_2

3.2. Radiation in two-phase ceramic composites

In this section, we illustrate the radiation scattering behavior of ceramic composites, consisting of RE pyrosilicates as the matrix phase and RE pyrochlores as embedded particles. The spectral absorption, scattering, and attenuation coefficients as well as the scattering phase functions are calculated using the Lorentz-Mie theory as detailed in Section 2. Fig. 2 illustrates a schematic profile of the ceramic composite, where each cubic micron of the partially absorbing matrix oxide is embedded with N particles of diameter D. The spectral absorption, scattering, and attenuation (or extinction) efficiency factors $(Q_{\lambda,a},Q_{\lambda,s},Q_{\lambda,e}=Q_{\lambda,a}+Q_{\lambda,s})$ and coefficients $(\sigma_{\lambda,a},\sigma_{\lambda,s},\beta_{\lambda})$ for all the ceramic composites are shown in Supplemental Figure S6. To compare the scattering behavior for different composite oxides, Fig. 3 illustrates the penetration length, which is the inverse of the extinction coefficient β , and the extinction efficiency factor $Q_e = Q_a + Q_s$ for different combinations of matrix oxide (RE2Si2O7) and particles (RE2Zr2O7 and RE₂Hf₂O₇). The average is calculated over the visible light and infrared spectrum, with wavelengths ranging from 0.4 to 3.3 µm, according to $\langle f \rangle = \frac{\int_{0.4}^{3.3} f d\lambda}{3.3-0.4}$.

By comparing Figs. 1(b) to 3, we note that ceramic composites with the largest mismatch between the refractive indices of the matrix and particle phases show the highest extinction efficiency factor

and the lowest penetration length. The penetration length of ceramic composites also dramatically decreases compared to the homogeneous media of individual pyrosilicate and pyrochlore phases, as shown in Fig. 4. This decrease is attributed to the significant contribution of interphase scattering between the medium oxide and the particle oxide, resulting from the introduced micro-structural inhomogeneities, which are absent in a homogeneous medium of oxides. We note that this observation is not general and depends on the size of the embedded particles in the composite (see more details in Section 3.3 and Supplemental Figures S10 and S11). To further illustrate the significant contribution of interphase interface scattering to the optical thickness of ceramic composites, Fig. 5 shows the single scattering albedo for different oxide composites. Single scattering albedo is defined as the ratio of scattering efficiency factor to the extinction efficiency factor, $Q_s/(Q_s+Q_a)$ and characterizes extinction by scattering relative to total extinction. For a purely scattering medium, the single scattering albedo is equal to 1. As shown in Fig. 5, the scattering albedo for all the studied composites are above 80% with the majority around 90%. Supplemental Figure S7 shows the contribution of absorption and scattering to the attenuation coefficient for different oxide composites. Tm₂Si₂O₇-Gd₂Zr₂O₇ and Gd₂Si₂O₇-Dy₂Hf₂O₇ exhibit the largest and smallest attenuation coefficients averaged over the visible and infrared

To fully understand the scattering behavior, we calculate the scattering phase function, $\Phi(\theta)$, for different composites. The scattering phase function profile shows the distribution of scattered radiation intensity as a function of scattering angle. The scattering phase function profile for each composite varies with the incident wavelength due to the changes in the interaction of the electromagnetic wave and the particle. Fig. 6 displays the scattering phase function for $Tm_2Si_2O_7-Gd_2Zr_2O_7$ and $Gd_2Si_2O_7-Dy_2Hf_2O_7$, which exhibit the largest and smallest attenuation coefficients among the studied composites, respectively (refer to Supplemental Figure S7), at two different wavelengths of radiation. For a given composite, the angular distribution of scattered radiation varies significantly with the incident wavelength, as evident by comparing Fig. 6(a) and (b) or (c) and (d). However, the scattering patterns for $Tm_2Si_2O_7-Gd_2Zr_2O_7$ and $Gd_2Si_2O_7-Dy_2Hf_2O_7$ are similar despite the large difference in their total attenuation coefficients.

To better understand the angular distribution of scattered radiation at each wavelength, we calculate the anisotropy factor. The scattering profile asymmetry (or anisotropy factor) quantifies the average cosine of the scattering angle and provides information about the average direction of scattering at each wavelength. If asymmetry is close to 0, the scattering is isotropic or equal in all directions, while a positive scattering asymmetry indicates that more scattering happens in the same direction as the incident radiation (a negative value shows that scattering is biased towards the opposite direction). Fig. 7 illustrates the spectral scattering asymmetry over the visible and infrared range for $\text{Tm}_2\text{Si}_2\text{O}_7\text{-Gd}_2\text{Zr}_2\text{O}_7$ and $\text{Gd}_2\text{Si}_2\text{O}_7\text{-Dy}_2\text{Hf}_2\text{O}_7$. The scattering pattern in terms of the wavelength for these two composites are very similar.

Our investigation reveals a consistent scattering profile pattern across various composite combinations, despite significant variations in the scattering efficiency factor for different matrix and particle oxide combinations (refer to Fig. 3). This similarity in the scattering pattern is further evidenced by the consistent scattering asymmetry observed in different composites, as illustrated in Supplemental Figure S8. In general, the scattering profile tends to approach a value close to one within the shorter wavelengths (i.e., the visible light range), gradually becoming more isotropic as the wavelength extends into the infrared range. The shift toward a more isotropic behavior is characterized by the asymmetry values approaching zero, with a value of zero indicating a fully spherical profile.

As shown earlier in Fig. 3, ceramic composites with the largest mismatch between the refractive indices of the matrix and particle phases show the highest extinction efficiency factor and the lowest penetration length averaged over the visible light and infrared range.

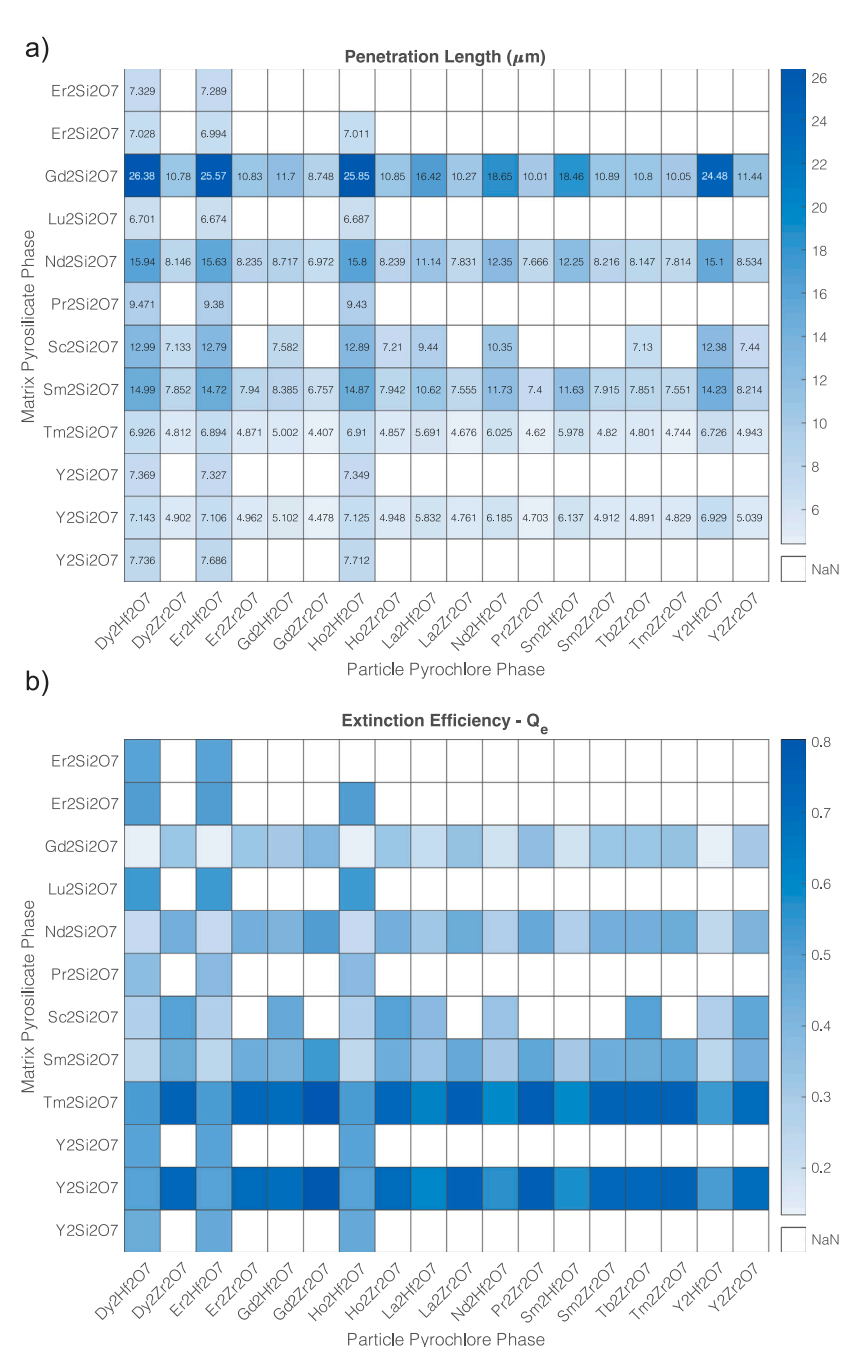


Fig. 3. The average (a) penetration length and (b) extinction efficiency factor for different combinations of matrix oxide $(Re_2Si_2O_7)$ and particles $(Re_2Zr_2O_7)$ and $Re_2Hf_2O_7)$ in the visible light and infrared range. Pairs of pyrosilicate and pyrochlores that are not included in the calculation are shown by white. Each cubic micron of the matrix phase contains one particle with a diameter of 0.6 μ m (N = 1, D = 0.6 μ m).

To better understand the determining factor in increasing the attenuation coefficient in ceramic composite, we investigate the relationship between radiation attenuation and refractive index mismatch between the two oxide phases in the composite. Fig. 8 shows the average penetration length and the average attenuation efficiency factor for different composites in terms of the refractive index mismatch of their constituent particles and matrix oxide phases. There is a clear correlation between the refractive index mismatch and radiation attenuation in the composite, where by increasing the mismatch, the attenuation become more significant (or the ceramic composite becomes more opaque).

To gain insights into the radiative flux behavior within various composites, we compute the Rosseland mean attenuation coefficient $(β_R)$ and the radiative conductivity (k_r) as functions of temperature for different composite materials as shown in Supplemental Figure S9. For example, we examine the radiative conductivities for ${\rm Tm_2Si_2O_7}$ – ${\rm Gd_2Zr_2O_7}$ and ${\rm Gd_2Si_2O_7}$ – ${\rm Dy_2Hf_2O_7}$, which exhibit the largest and smallest attenuation coefficients over the visible and infrared range, as shown earlier in Supplemental Figure S7. The effective radiative conductivity at 1782 K (slightly above 1500 °C) for ${\rm Tm_2Si_2O_7}$ – ${\rm Gd_2Zr_2O_7}$ and ${\rm Gd_2Si_2O_7}$ – ${\rm Dy_2Hf_2O_7}$ is calculated as 0.07 W m⁻¹ K⁻¹ and 0.35 W m⁻¹ K⁻¹, respectively. The calculated k_r for ${\rm Tm_2Si_2O_7}$ – ${\rm Gd_2Zr_2O_7}$ is approximately five times smaller than that for ${\rm Gd_2Si_2O_7}$ – ${\rm Dy_2Hf_2O_7}$, as expected due to the larger attenuation coefficient of the former. Fig. 9 illustrates $β_R$ and k_r for all the calculated composites at 1782 K. We also investigate the impact of refractive index mismatch between

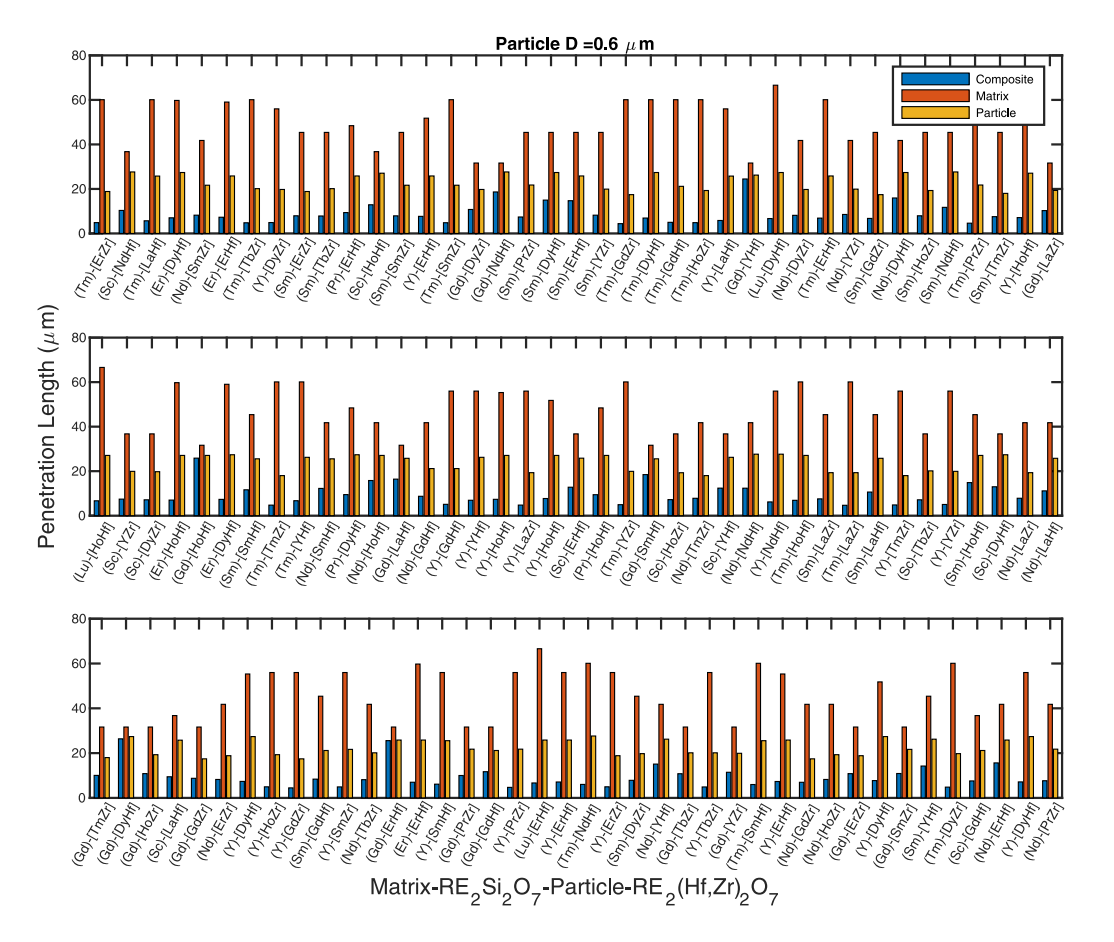


Fig. 4. The average penetration length (over visible and infrared range) for the composite oxide (matrix+particle) compared with the average penetration length of homogeneous media for the matrix and particle oxides separately. Each cubic micron of the matrix phase contains one particle with a diameter of 0.6 μ m (N = 1, D = 0.6 μ m).

the constituent particle and matrix oxides on both the local Rosseland mean attenuation coefficient and the effective radiative conductivity of these composites. Fig. 10 illustrates a strong correlation between the Rosseland mean attenuation coefficient (and, similarly, the radiative conductivity) and the refractive index mismatch of the constituent particle and matrix phase. By increasing the refractive mismatch between the particle and matrix oxides, the ceramic composite becomes more opaque, showing larger attenuation coefficient and smaller effective radiative conductivity.

3.3. Effect of particle size on radiation of composites

We also investigate the impact of particle size on the radiation behavior of the pyrosilicate–pyrochlore composites. Modifying the size of embedded particles significantly alters the scattering and attenuation characteristics within the composite. As shown in Fig. 11, the attenuation efficiency factor Q_e largely increases by increasing the embedded particle diameter. This behavior is expected because increasing the particle size increases the size parameter of the scatterer. The size parameter is defined as the ratio of the perimeter of a spherical particle (or scatterer) with diameter D to the wavelength of incident radiation inside the medium, λ_m . The extinction efficiency approaches 2 for very large size parameters in the geometric optics regime, a phenomenon known as the extinction paradox [62]. The range of size parameters in this study remains within the transition regime, where the particle size and the wavelength of incident radiation are in the same order. As shown in Fig. 11(a), the extinction efficiency factor exceeds values

of 1 for particle diameters greater than 0.8 μ m, indicating that the particle can attenuate more energy than its actual physical size because of energy diffraction around the particle. As shown in Section 3.2, the variation of Q_e among composites with the same particle size is largely determined by the refractive index mismatch between the particle and the matrix oxide.

As shown in Fig. 11(a), the attenuation efficiency factor for particle sizes of 0.2 μm are relatively small, with most composites reaching values close to zero. This implies that these particles are in effect not contributing to attenuation of radiation. This leads to attenuation coefficients of the composite to become smaller than individual homogeneous media of the matrix and particle oxides. As shown in Fig. 4, for particles of diameter 0.6 μm , the penetration length of ceramic composites decreases compared to the homogeneous media of individual matrix and particle phases. However, for smaller particle sizes of 0.2 and 0.4 μm , the penetration length of ceramic composites is larger than the individual homogeneous media of oxides because of fractional attenuation efficiency factor (see Supplemental Figure S10), indicating that embedding particles of these sizes has a detrimental effect on radiation mitigation.

Aside from the expected increase of the attenuation efficiency factor of the particle as its size increases, we observe that the scattering albedo largely decreases for smaller particles. In other words, by increasing the particle size, the contribution of scattering to the total attenuation of radiation increases. As shown in Fig. 11(b), the scattering albedo approaches to values above 90% for particles with a diameter larger

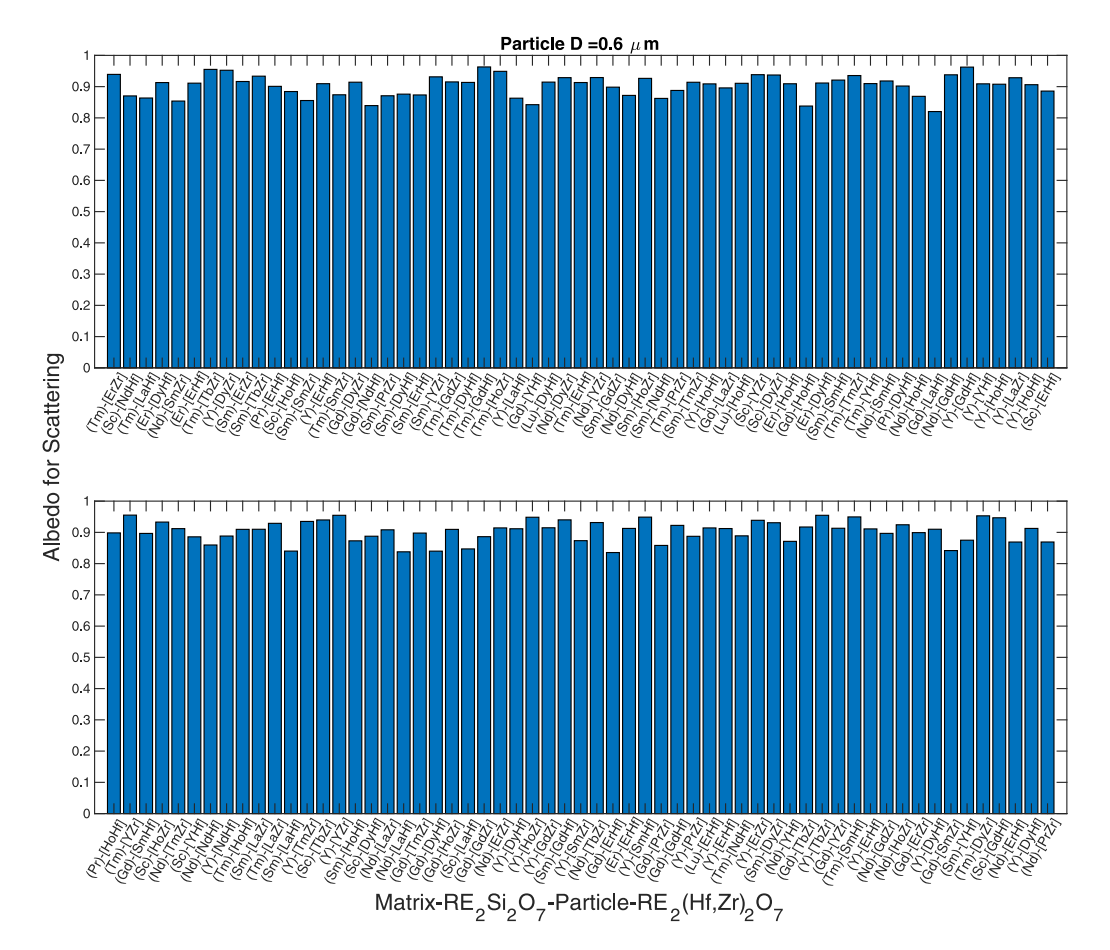


Fig. 5. The single scattering albedo for different composite oxides averaged over the visible and infrared range. Each cubic micron of the matrix phase contains one particle with a diameter of 0.6 μ m ($N = 1, D = 0.6 \mu$ m).

than 0.8 $\mu m.$ Supplemental Figure S11 shows the contribution of absorption and scattering to the attenuation coefficient for different particle sizes.

As shown in Fig. 12(a), the Rosseland mean attenuation coefficient increases significantly with increasing the particle diameter. This is a direct result of the increase in the attenuation efficiency factor. Consequently, the effective radiative conductivity decreases by increasing the particle size, as shown in Fig. 12(b). Fig. 13 illustrates the strong dependence of the extinction efficiency, Rosseland attenuation coefficient, and the effective radiative conductivity on both the size of the particles in the composite and the refractive index mismatch between the matrix and particle oxides.

We note that as the particle size becomes larger, the range of incident wavelength for which the independent scatterer assumption remains valid become smaller. According to $c+0.1D>\frac{1}{2}\lambda_m$, for particles of size 0.2, 0.4, 0.6, 0.8, 1 μ m, the wavelengths for which independent scatterer assumption remains valid are those smaller than 5.02, 4.19, 3.52, 2.57, 1.64 μ m, respectively. Note that as the particle size increases, the clearance distance c decreases. Given that the relevant operating temperature for thermal coatings reaches above 1500 °C, the blackbody emissivity derivative in Eq. (4) becomes negligible for wavelength values in the infrared range (see Supplemental Figure S12). Therefore, the calculated Rosseland mean attenuation and radiative conductivity based on the independent scatterer assumption are valid.

4. Discussion

We conduct a high-throughput investigation of radiative properties in rare-earth pyrosilicate–pyrochlore composites, with the pyrochlore serving as the particle phase and the pyrosilicate as the matrix. By studying 118 different composites with varying particle sizes, we demonstrate that thermal radiation can be significantly suppressed by increasing the optical mismatch between the matrix and particle oxides. Furthermore, increasing the size of embedded particles in the matrix contributes to additional thermal radiation mitigation.

Our theoretical investigation has its limitations. First and foremost, this study solely focuses on exploring the impact of refractive index mismatch between phases on radiation scattering within the composite. Hence, other influential factors such as grain boundaries, particle shape irregularities, impurities, or other microstructural defects, which can considerably affect radiation, have not been taken into account. Additionally, the level of theory employed in this study has inherent limitations. For instance, the underlying assumption of independent scatterers in our theoretical framework restricts our investigation to particle sizes smaller than 1 μ m per cubic micron of the matrix. For a more comprehensive modeling of arbitrary shapes of second-phase particles or irregular-shaped grains in the microstructure, more sophisticated numerical models such as the T-matrix approach [63], the discrete dipole approximation (DDA) [64], or Monte Carlo simulations [65,66] should be considered.

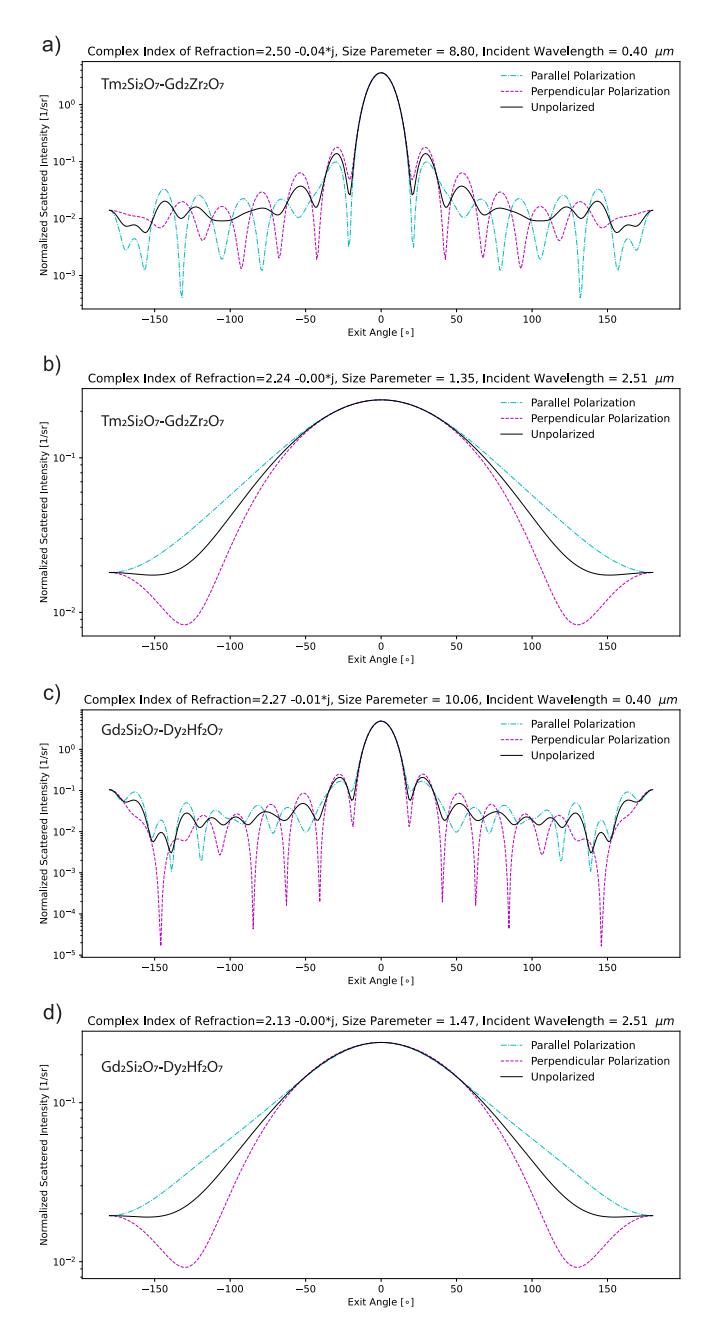


Fig. 6. The scattering phase function at two different incident wavelengths. The angular distribution of scattered radiation intensity for $Tm_2Si_2O_7-Gd_2Zr_2O_7$ at an incident radiation with (a) 0.4 μ m and (b) 2.51 μ m wavelengths, and for $Gd_2Si_2O_7-Dy_2Hf_2O_7$ at an incident radiation with (c) 0.4 μ m and (d) 2.51 μ m wavelengths. Each cubic micron of the matrix phase contains one particle with a diameter of 0.6 μ m (N=1,D=0.6 μ m). The scattering distribution for unpolarized and polarized incident radiation into perpendicular and parallel components are shown with different colors. (For interpretation of the references to color in this figure legend, the reader is referred to the web version of this article.)

Declaration of competing interest

The authors declare that they have no known competing financial interests or personal relationships that could have appeared to influence the work reported in this paper.

Acknowledgments

We would like to express our gratitude for the valuable insights shared during our discussions with Prof. Nitin Padture, who initially proposed the investigation into the role of optical mismatch in rareearth pyrosilicate composites for thermal radiation mitigation. This work was supported by the National Science Foundation (NSF) DMR-1954621. This work used Stampede2 at Texas Advanced Computing

Center through allocation MAT200013 from the Extreme Science and Engineering Discovery Environment (XSEDE), which was supported by National Science Foundation, United States grant number 1548562 and from Advanced Cyberinfrastructure Coordination Ecosystem: Services & Support (ACCESS) program, which is supported by National Science Foundation, United States grants 2138259, 2138286, 2138307, 2137603, and 2138296.

Appendix A. Supplementary data

Supplementary material related to this article can be found online at https://doi.org/10.1016/j.ceramint.2024.01.417.

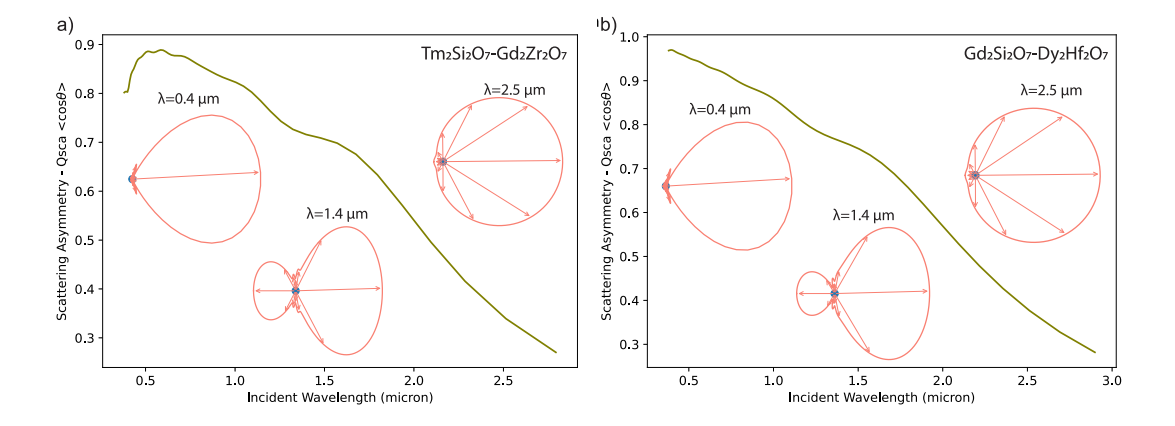


Fig. 7. The scattering asymmetry (or anisotropy factor) for (a) $\text{Tm}_2\text{Si}_2\text{O}_7$ – $\text{Gd}_2\text{Zr}_2\text{O}_7$ and (b) $\text{Gd}_2\text{Si}_2\text{O}_7$ – $\text{Dy}_2\text{Hf}_2\text{O}_7$ composites with $N=1, D=0.6~\mu\text{m}$, shown over the visible and infrared range. The insets indicate the scattering profile for different wavelengths.

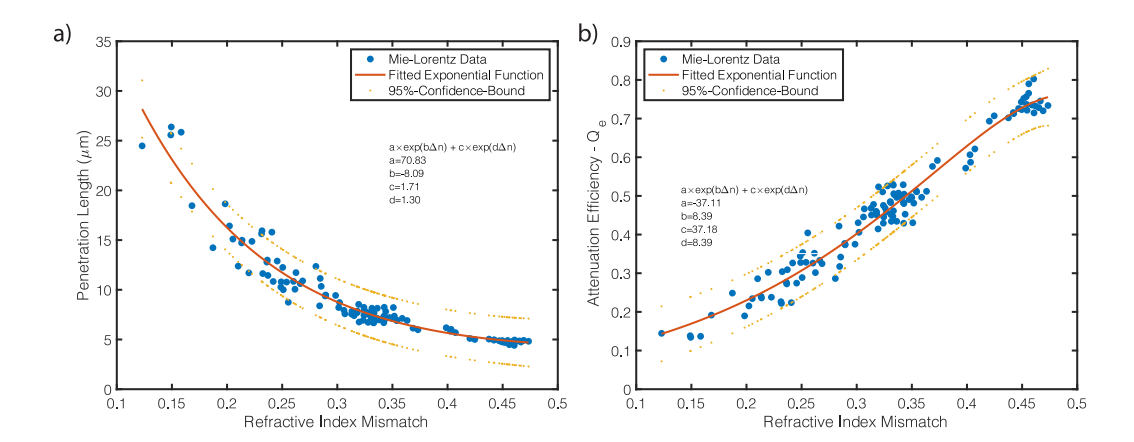


Fig. 8. Average (a) penetration length and (b) extinction efficiency factor over the visible light and infrared range versus the refractive index mismatch between the matrix and particle oxides for different composites. Each cubic micron of the matrix phase contains one particle with a diameter of $0.6 \ \mu m$ ($N = 1, D = 0.6 \ \mu m$).

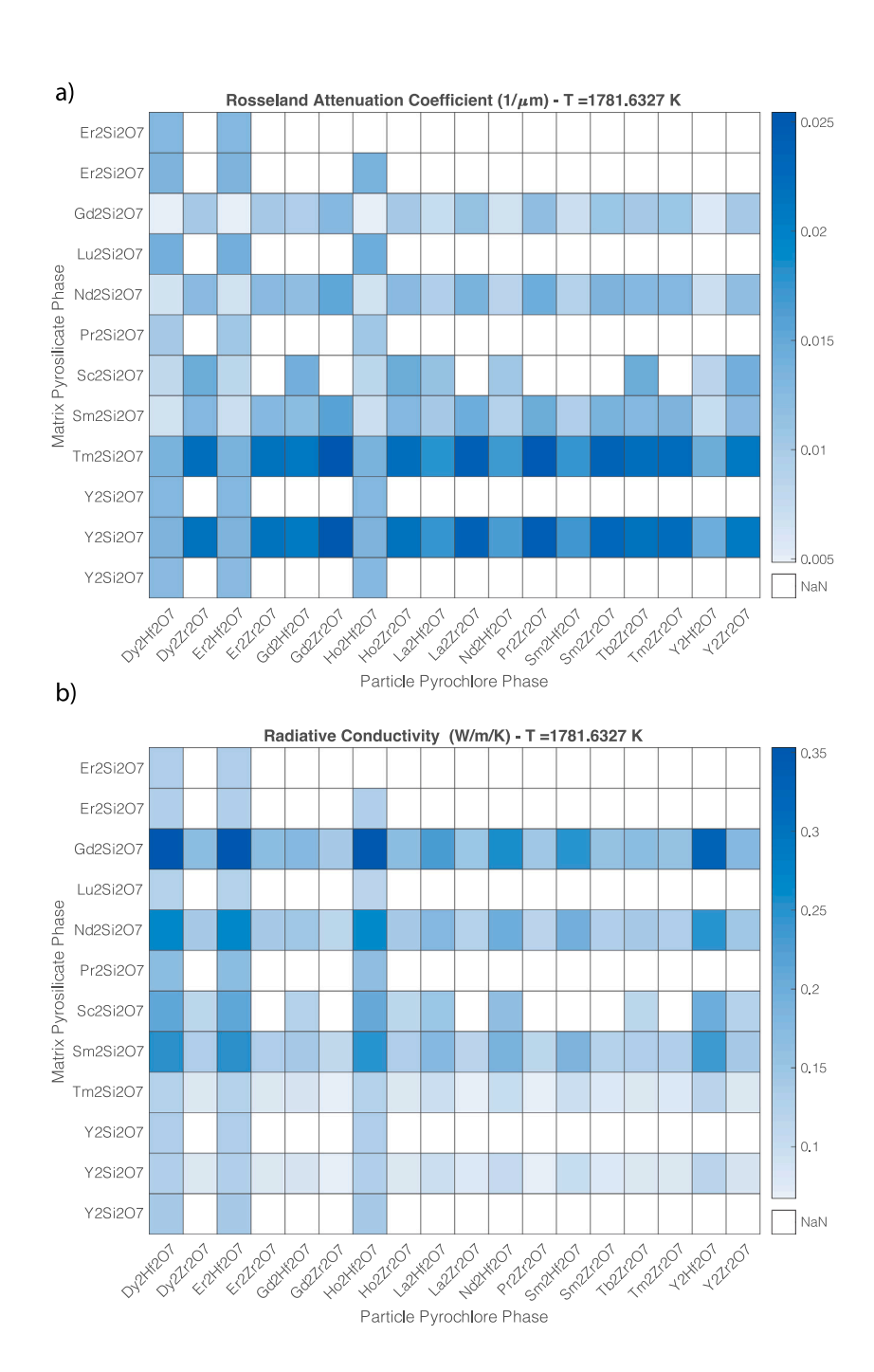


Fig. 9. (a) Rosseland mean attenuation coefficient and (b) effective radiative conductivity for different combinations of matrix oxide ($RE_2Si_2O_7$) and particles ($RE_2Zr_2O_7$ and $RE_2Hf_2O_7$) calculated at 1782 K. Pairs of pyrosilicate and pyrochlores that are not included in the calculation are shown by white. Each cubic micron of the matrix phase contains one particle with a diameter of 0.6 μ m (N = 1, D = 0.6 μ m).

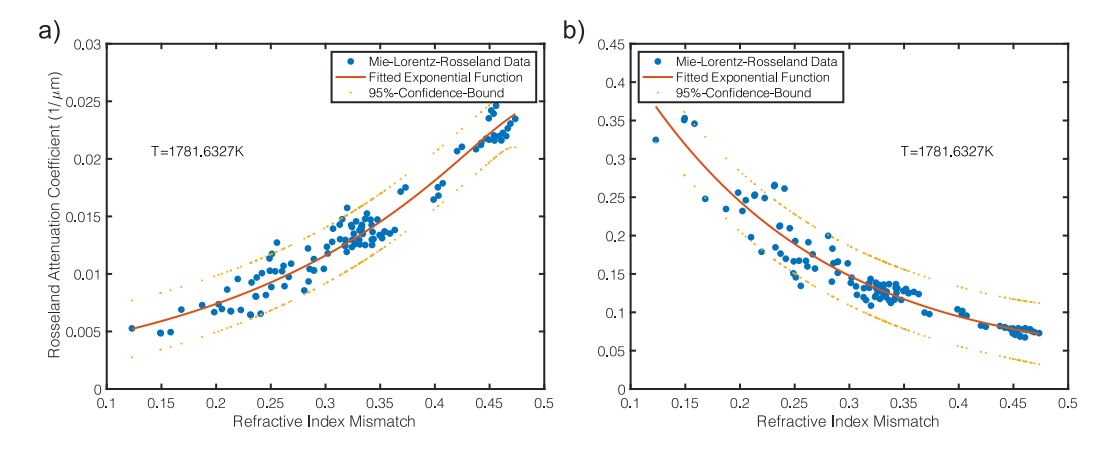


Fig. 10. (a) Rosseland mean attenuation coefficient and (b) effective radiative conductivity k_r at T=1782 K versus the refractive index mismatch between the matrix and particle oxides for different composites. Each cubic micron of the matrix phase contains one particle with a diameter of 0.6 μ m (N=1,D=0.6 μ m).

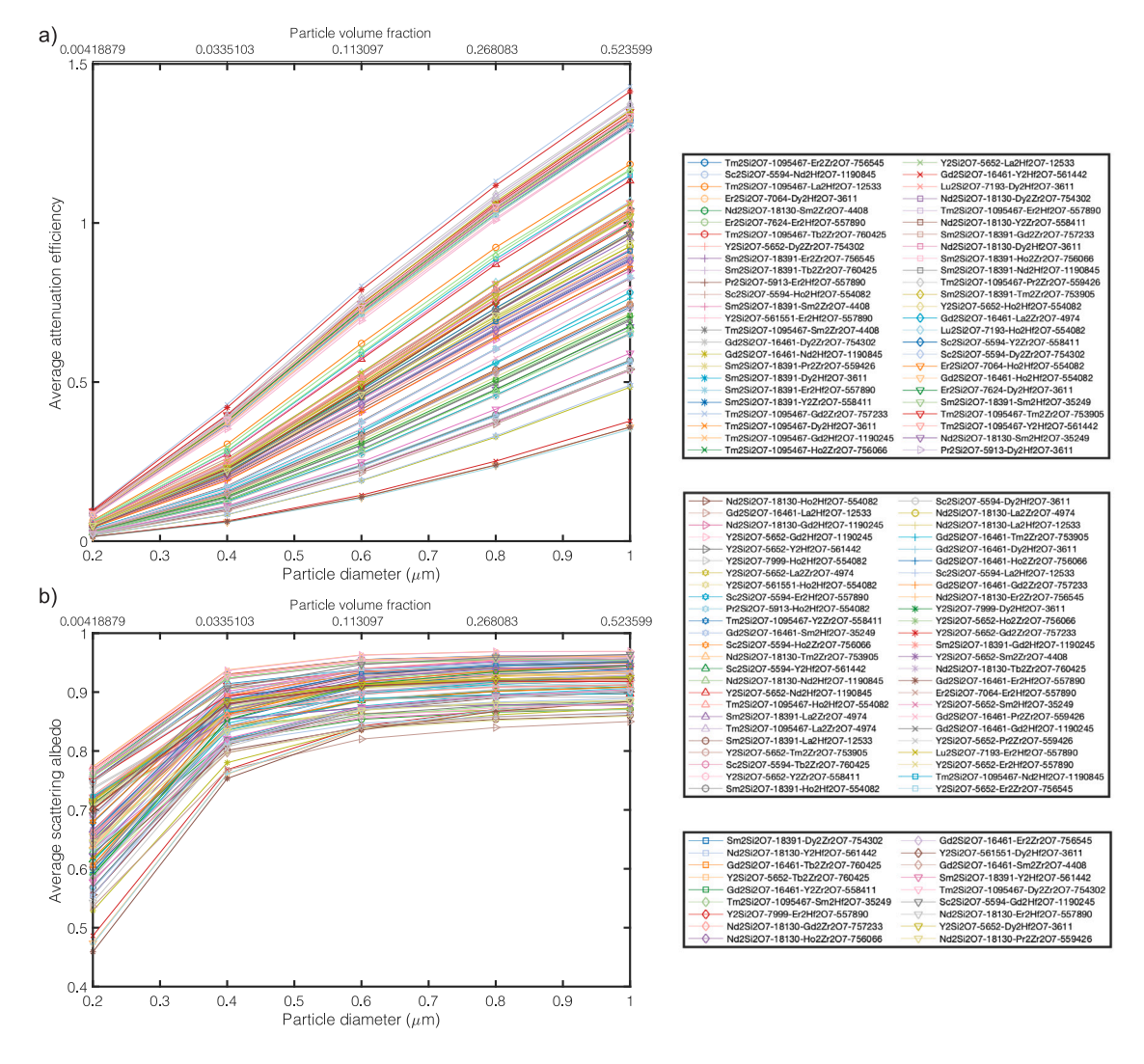


Fig. 11. (a) Average attenuation (or extinction) efficiency factor and (b) scattering albedo over visible and infrared range versus particle diameter in the composite. The legend indicates the matrix and particle combination with their corresponding Materials Project identification numbers. Each cubic micron of the matrix phase contains one particle.

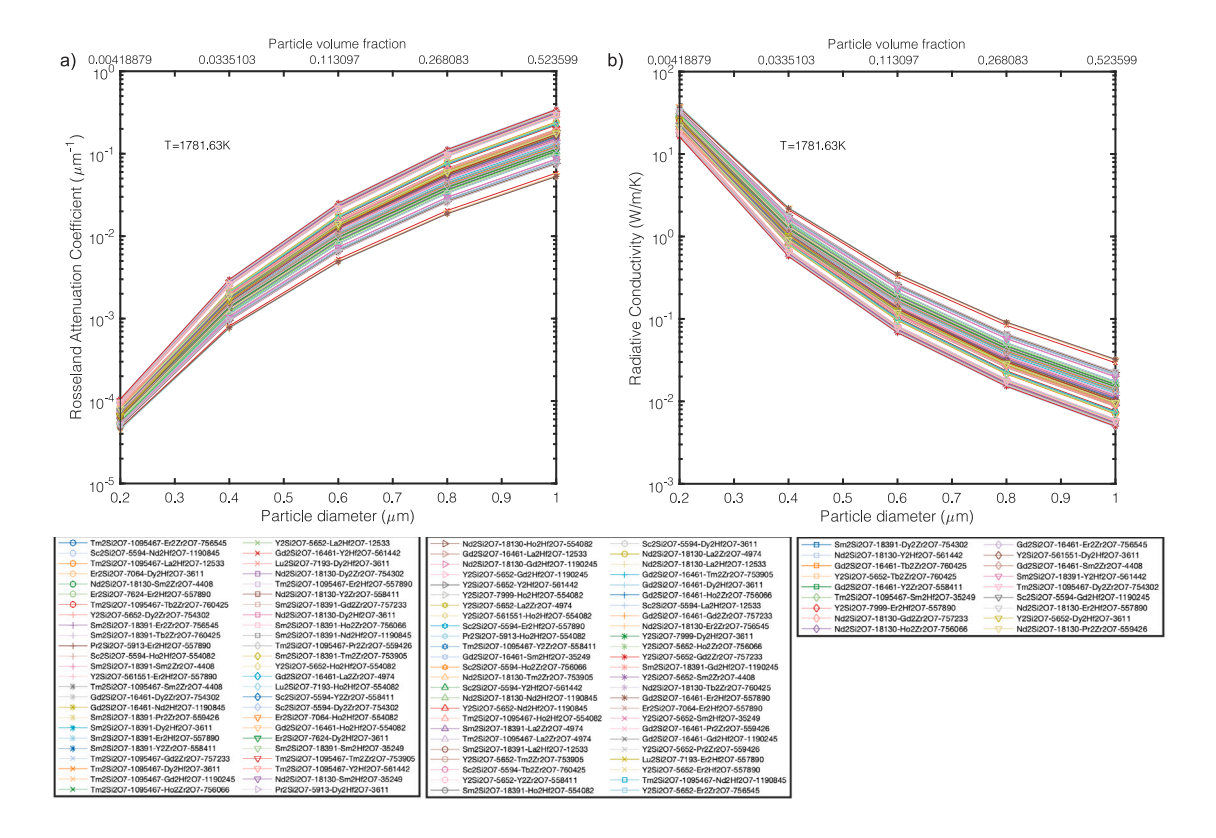
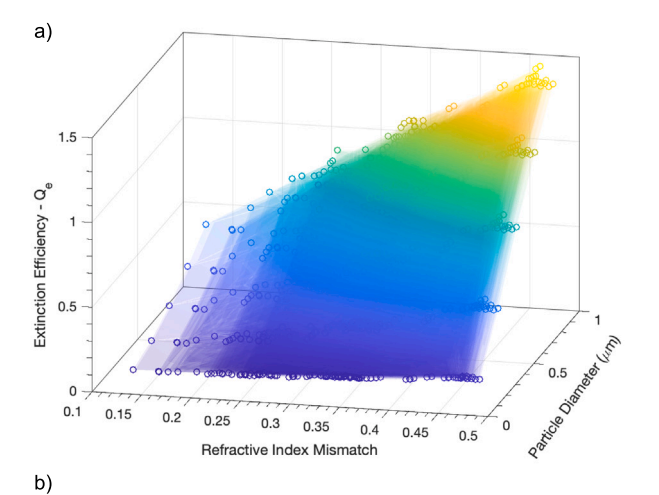
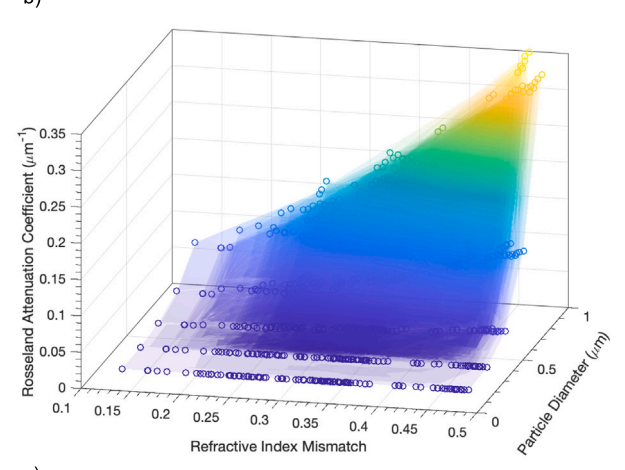


Fig. 12. (a) Rosseland mean attenuation coefficient and (b) effective radiative conductivity k_r at T=1782 K (≈ 1500 °C) versus particle diameter in the composite. The legend indicates the matrix and particle combination with their corresponding Materials Project identification numbers. Each cubic micron of the matrix phase contains one particle.





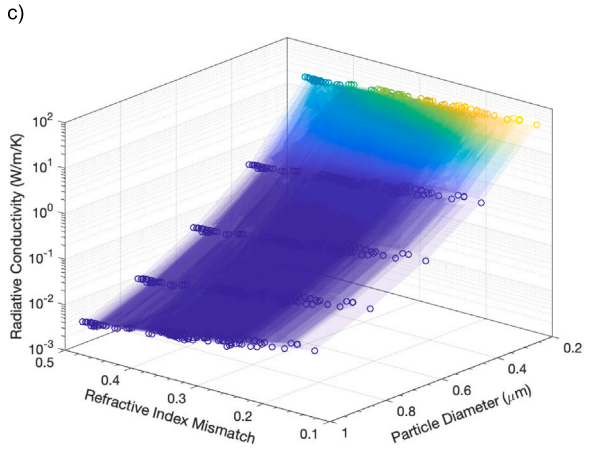


Fig. 13. (a) Average attenuation efficiency factor across the visible and infrared spectrum, (b) Rosseland mean attenuation coefficient at T=1782 K, and (c) effective radiative conductivity at T=1782 K depicted in relation to the particle diameter and refractive index mismatch between the particle and matrix oxides. Each cubic micron of the matrix phase encompasses one particle.

References

- Nitin P. Padture, Maurice Gell, Eric H. Jordan, Thermal barrier coatings for gas-turbine engine applications, Science (ISSN: 0036-8075) 296 (5566) (2002) 280–284, http://dx.doi.org/10.1126/science.1068609, https://science.sciencemag.org/content/296/5566/280.
- [2] Robert Vassen, Alexandra Stuke, Detlev Stöver, Recent developments in the field of thermal barrier coatings, J. Therm. Spray Technol. (ISSN: 1544-1016) 18 (2) (2009) 181–186, http://dx.doi.org/10.1007/s11666-009-9312-7.

- [3] David R. Clarke, Matthias Oechsner, Nitin P. Padture, Thermal-barrier coatings for more efficient gas-turbine engines, MRS Bull. (ISSN: 1938-1425) 37 (10) (2012) 891–898, http://dx.doi.org/10.1557/mrs.2012.232.
- [4] Daniel Tejero-Martin, Chris Bennett, Tanvir Hussain, A review on environmental barrier coatings: History, current state of the art and future developments, J. Eur. Ceram. Soc. (ISSN: 0955-2219) 41 (3) (2021) 1747–1768, http://dx.doi.org/10.1016/j.jeurceramsoc.2202.010.057, https://www.sciencedirect.com/science/article/pii/S0955221920308700.
- [5] D.R. Clarke, C.G. Levi, Materials design for the next generation thermal barrier coatings, Annu. Rev. Mater. Res. 33 (1) (2003) 383–417, http://dx.doi.org/10. 1146/annurev.matsci.33.011403.113718.
- [6] X.Q. Cao, R. Vassen, D. Stoever, Ceramic materials for thermal barrier coatings, J. Eur. Ceram. Soc. (ISSN: 0955-2219) 24 (1) (2004) 1–10, http://dx.doi.org/10.1016/S0955-2219(03)00129-8, http://www.sciencedirect.com/science/article/pii/S0955221903001298.
- [7] Carlos G. Levi, Emerging materials and processes for thermal barrier systems, Curr. Opin. Solid State Mater. Sci. (ISSN: 1359-0286) 8 (1) (2004) 77-91, http://dx.doi.org/10.1016/j.cossms.2004.03.009, http://www.sciencedirect.com/science/article/pii/S1359028604000385.
- [8] Jie Wu, Xuezheng Wei, Nitin P. Padture, Paul G. Klemens, Maurice Gell, Eugenio García, Pilar Miranzo, Maria I. Osendi, Low-thermal-conductivity rare-earth zirconates for potential thermal-barrier-coating applications, J. Am. Ceram. Soc. 85 (12) (2002) 3031–3035, http://dx.doi.org/10.1111/j.1151-2916.2002.tb00574.x, https://ceramics.onlinelibrary.wiley.com/doi/abs/10.1111/j.1151-2916.2002.tb00574.x.
- [9] G.A. Slack, The thermal conductivity of nonmetallic crystals, J. Phys. C: Solid State Phys. 34 (1979) 1–71.
- [10] D.G. Cahill, R.O. Pohl, Lattice vibrations and heat transport in crystals and glasses, Ann. Rev. Phys. Chem. 39 (1) (1988) 93–121, http://dx.doi.org/10.1146/ annurev.pc.39.100188.000521.
- [11] David G. Cahill, S.K. Watson, R.O. Pohl, Lower limit to the thermal conductivity of disordered crystals, Phys. Rev. B 46 (1992) 6131–6140, http://dx.doi.org/10. 1103/PhysRevB.46.6131, https://link.aps.org/doi/10.1103/PhysRevB.46.6131.
- [12] Michael R. Winter, David R. Clarke, Oxide materials with low thermal conductivity, J. Am. Ceram. Soc. 90 (2) (2007) 533–540, http://dx.doi.org/10.1111/j.1551-2916.2006.01410.x, https://ceramics.onlinelibrary.wiley.com/doi/abs/10.1111/j.1551-2916.2006.01410.x.
- [13] David R. Clarke, Materials selection guidelines for low thermal conductivity thermal barrier coatings, Surf. Coat. Technol. (ISSN: 0257-8972) 163–164 (2003) 67–74, http://dx.doi.org/10.1016/S0257-8972(02)00593-5, http://www. sciencedirect.com/science/article/pii/S0257897202005935. Proceedings of the 29th International conference on Metallurgical Coatings and Thin Films.
- [14] Wei Pan, Simon R. Phillpot, Chunlei Wan, Aleksandr Chernatynskiy, Zhixue Qu, Low thermal conductivity oxides, MRS Bull. (ISSN: 1938-1425) 37 (10) (2012) 917–922, http://dx.doi.org/10.1557/mrs.2012.234.
- [15] Nitin P. Padture, Advanced structural ceramics in aerospace propulsion, Nature Mater. (ISSN: 1476-4660) 15 (8) (2016) 804–809, http://dx.doi.org/10.1038/nmat4687.
- [16] W.A. Ge, C.Y. Zhao, B.X. Wang, Thermal radiation and conduction in functionally graded thermal barrier coatings. Part I: Experimental study on radiative properties, Int. J. Heat Mass Transfer (ISSN: 0017-9310) 134 (2019) 101– 113, http://dx.doi.org/10.1016/j.ijheatmasstransfer.2019.01.018, https://www. sciencedirect.com/science/article/pii/S0017931018346908.
- [17] I.O. Golosnoy, S.A. Tsipas, T.W. Clyne, An analytical model for simulation of heat flow in plasma-sprayed thermal barrier coatings, J. Therm. Spray Technol. (ISSN: 1544-1016) 14 (2) (2005) 205–214, http://dx.doi.org/10.1361/ 10599630523764.
- [18] Leire del Campo, Domingos De Sousa Meneses, Karine Wittmann-Ténèze, Antoine Bacciochini, Alain Denoirjean, Patrick Echegut, Effect of porosity on the infrared radiative properties of plasma-sprayed Yttria-stabilized Zirconia ceramic thermal barrier coatings, J. Phys. Chem. C (ISSN: 1932-7447) 118 (25) (2014) 13590–13597, http://dx.doi.org/10.1021/jp5014362.
- [19] I.O Golosnoy, A Cipitria, T.W. Clyne, Heat transfer through plasma-sprayed thermal barrier coatings in gas turbines: A review of recent work, J. Therm. Spray Technol. (ISSN: 1544-1016) 18 (5) (2009) 809–821, http://dx.doi.org/10. 1007/s11666-009-9337-y.
- 20] Jun Yang, Chunlei Wan, Meng Zhao, Muhammad Shahid, Wei Pan, Effective blocking of radiative thermal conductivity in La2Zr2O7/LaPO4 composites for high temperature thermal insulation applications, J. Eur. Ceram. Soc. (ISSN: 0955-2219) 36 (15) (2016) 3809–3814, http://dx.doi.org/10.1016/j.jeurceramsoc.2016.03.010, https://www.sciencedirect.com/science/article/pii/S0955221916301145. Preparation and Application of Ultra-high Temperature Ceramic Matrix Composites.
- [21] Muzhang Huang, Jia Liang, Peng Zhang, Yi Li, Yi Han, Zesheng Yang, Wei Pan, Chunlei Wan, Opaque gd2zr2o7/gdmno3 thermal barrier materials for thermal radiation shielding: The effect of polaron excitation, J. Mater. Sci. Technol. (ISSN: 1005-0302) 100 (2022) 67–74, http://dx.doi.org/10.1016/j.jmst.2021.06.013, https://www.sciencedirect.com/science/article/pii/S1005030221006095.

- [22] J. Manara, M. Arduini-Schuster, H.-J. Rätzer-Scheibe, U. Schulz, Infrared-optical properties and heat transfer coefficients of semitransparent thermal barrier coatings, Surf. Coat. Technol. (ISSN: 0257-8972) 203 (8) (2009) 1059–1068, http://dx.doi.org/10.1016/j.surfcoat.2008.09.033, https://www.sciencedirect.com/science/article/pii/S0257897208009638.
- [23] Robert Siegel, Internal radiation effects in zirconia thermal barrier coatings, J. Thermophys. Heat Transfer 10 (4) (1996) 707–709, http://dx.doi.org/10.2514/ 3.851
- [24] Leonid A. Dombrovsky, Herve Kamdem Tagne, Dominique Baillis, Laurent Gremillard, Near-infrared radiative properties of porous zirconia ceramics, Infrared Phys. Technol. (ISSN: 1350-4495) 51 (1) (2007) 44–53, http://dx.doi.org/ 10.1016/j.infrared.2006.11.003, https://www.sciencedirect.com/science/article/ pii/S1350449506001587.
- [25] Li Wang, Jeffrey I. Eldridge, S.M. Guo, Thermal radiation properties of plasma-sprayed gd2zr2o7 thermal barrier coatings, Scr. Mater. (ISSN: 1359-6462) 69 (9) (2013) 674–677, http://dx.doi.org/10.1016/j.scriptamat.2013.07.026, https://www.sciencedirect.com/science/article/pii/S1359646213003813.
- [26] B.X. Wang, C.Y. Zhao, Predicting radiative transport properties of plasma sprayed porous ceramics, J. Appl. Phys. 119 (12) (2016) 125110, http://dx.doi.org/10. 1063/1.4945031.
- [27] B.X. Wang, C.Y. Zhao, Effect of anisotropy on thermal radiation transport in porous ceramics, Int. J. Therm. Sci. (ISSN: 1290-0729) 111 (2017) 301–309, http://dx.doi.org/10.1016/j.ijthermalsci.2016.09.012, https://www.sciencedirect.com/science/article/pii/S1290072916303350.
- [28] Zhixue Qu, Taylor D. Sparks, Wei Pan, David R. Clarke, Thermal conductivity of the gadolinium calcium silicate apatites: Effect of different point defect types, Acta Mater. (ISSN: 1359-6454) 59 (10) (2011) 3841–3850, http://dx. doi.org/10.1016/j.actamat.2011.03.008, http://www.sciencedirect.com/science/ article/pii/S1359645411001558.
- [29] G. Yang, C.Y. Zhao, Infrared radiative properties of eb-pvd thermal barrier coatings, Int. J. Heat Mass Transfer (ISSN: 0017-9310) 94 (2016) 199–210, http://dx.doi.org/10.1016/j.ijheatmasstransfer.2015.11.063, https://www.sciencedirect.com/science/article/pii/S0017931015302799.
- [30] G. Yang, C.Y. Zhao, A comparative experimental study on radiative properties of EB-PVD and air plasma sprayed thermal barrier coatings, J. Heat Transfer (ISSN: 0022-1481) 137 (9) (2015) 091024, http://dx.doi.org/10.1115/1.4030243, 09.
- [31] H. Shi, C.Y. Zhao, B.X. Wang, Modeling the thermal radiation properties of thermal barrier coatings based on a random generation algorithm, Ceram. Int. (ISSN: 0272-8842) 42 (8) (2016) 9752–9761, http://dx.doi.org/10.1016/j.ceramint.2016.03.067, https://www.sciencedirect.com/science/article/pii/S0272884216302000.
- [32] Quentin Flamant, David R. Clarke, Opportunities for minimizing radiative heat transfer in future thermal and environmental barrier coatings, Scr. Mater. (ISSN: 1359-6462) 173 (2019) 26–31, http://dx.doi.org/10.1016/j.scriptamat.2019.07. 041, http://www.sciencedirect.com/science/article/pii/S135964621930449X.
- [33] Laura R. Turcer, Nitin P. Padture, Towards multifunctional thermal environmental barrier coatings (TEBCs) based on rare-earth pyrosilicate solid-solution ceramics, Scr. Mater. (ISSN: 1359-6462) 154 (2018) 111–117, http://dx.doi.org/10.1016/j.scriptamat.2018.05.032, http://www.sciencedirect.com/science/article/pii/S1359646218303269.
- [34] Laura R. Turcer, Arundhati Sengupta, Nitin P. Padture, Low thermal conductivity in high-entropy rare-earth pyrosilicate solid-solutions for thermal environmental barrier coatings, Scr. Mater. (ISSN: 1359-6462) 191 (2021) 40–45, http: //dx.doi.org/10.1016/j.scriptamat.2020.09.008, http://www.sciencedirect.com/ science/article/pii/S1359646220305972.
- [35] Hafiz Sartaj Aziz, Muzhang Huang, Zongyuan Li, Chunlei Wan, Wei Pan, Repressing high-temperature radiative heat transfer in thermal barrier coatings, J. Am. Ceram. Soc. 105 (5) (2022) 3485–3497, http://dx.doi.org/10.1111/jace.18321, https://ceramics.onlinelibrary.wiley.com/doi/abs/10.1111/jace.18321.
- [36] Qian Guo, Wenting He, Chun Li, Jian He, Jingyong Sun, Hongbo Guo, High-temperature interface stability of tri-layer thermal environmental barrier coatings, Ceram. Int. (ISSN: 0272-8842) 48 (7) (2022) 9313–9323, http://dx.doi.org/10.1016/j.ceramint.2021.12.124, https://www.sciencedirect.com/science/article/pii/S0272884221039055.
- [37] W. Kohn, L.J. Sham, Self-consistent equations including exchange and correlation effects, Phys. Rev. 140 (1965) A1133–A1138, http://dx.doi.org/10.1103/PhysRev.140.A1133, https://link.aps.org/doi/10.1103/PhysRev.140.A1133.
- [38] G. Kresse, J. Hafner, Ab initio molecular dynamics for liquid metals, Phys. Rev. B 47 (1993) 558–561, http://dx.doi.org/10.1103/PhysRevB.47.558, https://link.aps.org/doi/10.1103/PhysRevB.47.558.
- [39] G. Kresse, J. Furthmüller, Efficiency of ab-initio total energy calculations for metals and semiconductors using a plane-wave basis set, Comput. Mater. Sci. (ISSN: 0927-0256) 6 (1) (1996) 15–50, http://dx.doi.org/10.1016/0927-0256(96)00008-0, https://www.sciencedirect.com/science/article/pii/ 0927025696000080.
- [40] G. Kresse, J. Furthmüller, Efficient iterative schemes for ab initio total-energy calculations using a plane-wave basis set, Phys. Rev. B 54 (1996) 11169– 11186, http://dx.doi.org/10.1103/PhysRevB.54.11169, https://link.aps.org/doi/ 10.1103/PhysRevB.54.11169.

- [41] P.E. Blöchl, Projector augmented-wave method, Phys. Rev. B 50 (1994) 17953– 17979, http://dx.doi.org/10.1103/PhysRevB.50.17953, https://link.aps.org/doi/ 10.1103/PhysRevB.50.17953.
- [42] G. Kresse, D. Joubert, From ultrasoft pseudopotentials to the projector augmented-wave method, Phys. Rev. B 59 (1999) 1758–1775, http://dx.doi. org/10.1103/PhysRevB.59.1758, https://link.aps.org/doi/10.1103/PhysRevB.59. 1758.
- [43] John P. Perdew, Kieron Burke, Matthias Ernzerhof, Generalized gradient approximation made simple, Phys. Rev. Lett. 77 (1996) 3865–3868, https://dx.doi.org/10.1103/PhysRevLett.77.3865, https://link.aps.org/doi/10.1103/PhysRevLett.77.3865.
- [44] M. Gajdoš, K. Hummer, G. Kresse, J. Furthmüller, F. Bechstedt, Linear optical properties in the projector-augmented wave methodology, Phys. Rev. B 73 (2006) 045112, http://dx.doi.org/10.1103/PhysRevB.73.045112, https://link.aps.org/doi/10.1103/PhysRevB.73.045112.
- [45] Hans Kuzmany, The Dielectric Function, Springer Berlin Heidelberg, Berlin, Heidelberg, ISBN: 978-3-662-03594-8, 1998, pp. 101–120, http://dx.doi.org/10. 1007/978-3-662-03594-8_6.
- [46] H. Ehrenreich, M.H. Cohen, Self-consistent field approach to the many-electron problem, Phys. Rev. 115 (1959) 786–790, http://dx.doi.org/10.1103/PhysRev. 115.786, https://link.aps.org/doi/10.1103/PhysRev.115.786.
- [47] David Bohm, David Pines, A collective description of electron interactions. i. magnetic interactions, Phys. Rev. 82 (1951) 625–634, http://dx.doi.org/10.1103/ PhysRev.82.625, https://link.aps.org/doi/10.1103/PhysRev.82.625.
- [48] A. Seidl, A. Görling, P. Vogl, J.A. Majewski, M. Levy, Generalized Kohn-Sham schemes and the band-gap problem, Phys. Rev. B 53 (1996) 3764–3774, http://dx.doi.org/10.1103/PhysRevB.53.3764, https://link.aps.org/doi/10.1103/PhysRevB.53.3764.
- [49] John P. Perdew, Kieron Burke, Matthias Ernzerhof, Generalized gradient approximation made simple, Phys. Rev. Lett. 77 (1996) 3865–3868, https://dx.doi.org/10.1103/PhysRevLett.77.3865, https://link.aps.org/doi/10.1103/PhysRevLett.77.3865.
- [50] Gustav Mie, Beiträge zur optik trüber medien, speziell kolloidaler metallösungen, Ann. Phys. 330 (3) (1908) 377–445, http://dx.doi.org/10. 1002/andp.19083300302, https://onlinelibrary.wiley.com/doi/abs/10.1002/andp.19083300302.
- [51] J.R. Howell, M.P. Menguc, R. Siegel, Thermal Radiation Heat Transfer, fifth ed., CRC Press, ISBN: 9781439894552, 2010, https://books.google.com/books?id= FBiSBOAAOBAJ.
- [52] Scott Prahl, Miepython, 2021, https://miepython.readthedocs.io/en/latest/index.
- [53] W.D. Kingery, Thermal conductivity: Xii, temperature dependence of conductivity for single-phase ceramics, J. Am. Ceram. Soc. 38 (7) (1955) 251–255, http:// dx.doi.org/10.1111/j.1151-2916.1955.tb14940.x, https://ceramics.onlinelibrary. wiley.com/doi/abs/10.1111/j.1151-2916.1955.tb14940.x.
- [54] D.W. Lee, W.D. Kingery, Radiation energy transfer and thermal conductivity of ceramic oxides, J. Am. Ceram. Soc. 43 (11) (1960) 594–607, http://dx.doi.org/ 10.1111/j.1151-2916.1960.tb13623.x, https://ceramics.onlinelibrary.wiley.com/ doi/abs/10.1111/j.1151-2916.1960.tb13623.x.
- [55] Donald V. Walters, Richard O. Buckius, Rigorous development for radiation heat transfer in nonhomogeneous absorbing, emitting and scattering media, Int. J. Heat Mass Transfer (ISSN: 0017-9310) 35 (12) (1992) 3323–3333, http://dx.doi.org/10.1016/0017-9310(92)90219-I, https://www.sciencedirect.com/science/article/pii/001793109290219I.
- [56] R. Siegel, C.M. Spuckler, Approximate solution methods for spectral radiative transfer in high refractive index layers, Int. J. Heat Mass Transfer (ISSN: 0017-9310) 37 (1994) 403–413, http://dx.doi.org/10.1016/0017-9310(94)90040-X, https://www.sciencedirect.com/science/article/pii/001793109490040X.
- [57] Robert Siegel, Charles M. Spuckler, Analysis of thermal radiation effects on temperatures in turbine engine thermal barrier coatings, Mater. Sci. Eng. A 245 (2) (1998) 150–159, http://dx.doi.org/10.1016/S0921-5093(97)00845-9, http://www.sciencedirect.com/science/article/pii/S0921509397008459.
- [58] Jeffrey I. Eldridge, Charles M. Spuckler, Determination of scattering and absorption coefficients for plasma-sprayed Yttria-stabilized Zirconia thermal barrier coatings, J. Am. Ceram. Soc. 91 (5) (2008) 1603–1611, http://dx.doi.org/10. 1111/j.1551-2916.2008.02349.x, https://ceramics.onlinelibrary.wiley.com/doi/abs/10.1111/j.1551-2916.2008.02349.x.
- [59] Jeffrey I. Eldridge, Charles M. Spuckler, James R. Markham, Determination of scattering and absorption coefficients for plasma-sprayed Yttria-stabilized Zirconia thermal barrier coatings at elevated temperatures, J. Am. Ceram. Soc. 92 (10) (2009) 2276–2285, http://dx.doi.org/10.1111/j.1551-2916.2009.03217.x, https: //ceramics.onlinelibrary.wiley.com/doi/abs/10.1111/j.1551-2916.2009.03217.x.
- [60] Yuji Kintaka, Takeshi Hayashi, Atsushi Honda, Masashi Yoshimura, Satoshi Kuretake, Nobuhiko Tanaka, Akira Ando, Hiroshi Takagi, Abnormal partial dispersion in pyrochlore lanthanum zirconate transparent ceramics, J. Am. Ceram. Soc. 95 (9) (2012) 2899–2905, http://dx.doi.org/10.1111/j.1551-2916.2012.05242.x, https://ceramics.onlinelibrary.wiley.com/doi/abs/10.1111/j.1551-2916.2012.05242.x.

ARTICLE IN PRESS

- [61] Guohong Zhou, Zhengjuan Wang, Bozhu Zhou, Yi Zhao, Guangjun Zhang, Shiwei Wang, Fabrication of transparent y2hf2o7 ceramics via vacuum sintering, Opt. Mater. (ISSN: 0925-3467) 35 (4) (2013) 774–777, http://dx.doi.org/10. 1016/j.optmat.2012.09.016, https://www.sciencedirect.com/science/article/pii/ S0925346712003898. 7th LCS.
- [62] H. Moosmüller, C.M. Sorensen, Single scattering albedo of homogeneous, spherical particles in the transition regime, J. Quant. Spectrosc. Radiat. Transfer (ISSN: 0022-4073) 219 (2018) 333–338, http://dx.doi.org/10.1016/j.jqsrt.2018.08.015, https://www.sciencedirect.com/science/article/pii/S0022407318305363.
- [63] M.I. Mishchenko, G. Videen, V.A. Babenko, N.G. Khlebtsov, T. Wriedt, T-matrix theory of electromagnetic scattering by particles and its applications: A comprehensive reference database, J. Quant. Spectrosc. Radiat. Transf. 88 (2004) 357–406, http://dx.doi.org/10.1016/j.jqsrt.2004.05.002.
- [64] Bruce T. Draine, Piotr J. Flatau, Discrete-dipole approximation for scattering calculations, J. Opt. Soc. Amer. A 11 (4) (1994) 1491–1499, http://dx.doi.org/10.1364/JOSAA.11.001491, http://josaa.osa.org/abstract.cfm? URI=josaa-11-4-1491.
- [65] J.R. Howell, The Monte Carlo method in radiative heat transfer, J. Heat Transfer (ISSN: 0022-1481) 120 (3) (1998) 547–560, http://dx.doi.org/10.1115/ 1.2824310, 08.
- [66] Michael F. Modest, Backward Monte Carlo simulations in radiative heat transfer , J. Heat Transfer (ISSN: 0022-1481) 125 (1) (2003) 57–62, http://dx.doi.org/ 10.1115/1.1518491, 1.